

Large enhancement of total reaction cross sections at the edge of the island of inversion in Ti, Cr, and Fe isotopes

W. Horiuchi,^{1,*} T. Inakura,² and S. Michimasa³

¹*Department of Physics, Hokkaido University, Sapporo 060-0810, Japan*

²*Laboratory for Zero-Carbon Energy, Institute of Innovative Research,
Tokyo Institute of Technology, Tokyo 152-8550, Japan*

³*Center for Nuclear Study, The University of Tokyo, 2-1 Hirosawa, Wako, Saitama 351-0198, Japan*

A systematic analysis of nuclear deformation is made for neutron-rich Ti, Cr, and Fe isotopes to explore the nuclear structure in the island of inversion near $N = 40$, where strong nuclear deformation is predicted. The nuclear ground states are obtained by the Skyrme Hartree-Fock method in three-dimensional coordinate space, which properly describes any nuclear shape. Three types of Skyrme interactions are employed to generate various deformed states in its isotopic chain. We find that in the island of inversion the occupation of highly elongated intruder orbits induces not only large quadrupole deformation but also large hexadecapole deformation. This appears as a sizable enhancement of the nuclear matter radius, showing the characteristic shell effect of the density profile near the nuclear surface. We show that the edge of the island of inversion, where the intruder orbit starts being occupied, can be determined by measuring the enhancement of the total reaction cross section at high incident energy. The possibility of constraining the hexadecapole deformation by a measurement of the total reaction cross sections is discussed.

I. INTRODUCTION

Recent theoretical and experimental studies on short-lived nuclei are addressing the nature of a proposed island of inversion region near $N = 40$, and suggest that nuclear stability enhances in neutron-rich isotones around ^{64}Cr [1] and ^{62}Ti [2]. A concept of the island of inversion [3] was first proposed to explain unexpected nature such as excess stabilization of atomic masses and low-lying first 2^+ energies of even-even nuclei around ^{32}Mg [4–6]. Similar scenarios were suggested to explain the onset of nuclear deformation in neutron-rich magic nuclei at $N = 8$ [7–9] and 28 [10–13]. Also, the Jahn-Teller stabilization at $N = 40$ was theoretically predicted [14]. Since this suggestion, many experimental results on the $N = 40$ island of inversion were reported: The systematics of the atomic masses [2, 15–17], low-lying excited states [18–24], and quadrupole collectivity [25, 26]. Despite the above experimental information in this mass region, the whole picture of the island of inversion near $N = 40$ is still uncertain such as divergence between the peaks of the mass stability and the quadrupole collectivity. Therefore, careful investigations through various observables are crucially important.

Strong nuclear deformation is one of the most prominent indications of the island of inversion. In this paper, the edge of the island of inversion near $N = 40$ is defined as the occupation of the intruder orbit stemming from the spherical $0g_{9/2}$ orbit, leading to large deformation, which is a natural extension of the island of inversion near $N = 20$, where the intruder orbit from the spherical $0f_{7/2}$ orbit is occupied. We remark that the effect of the configuration mixing around ^{64}Cr was discussed

in detail [1]. To know the structure information on the occupation of the intruder orbits related to fp - and gds -configuration mixing, it is more advantageous to study observables such as transition probabilities and nuclear radii.

Generally, the direct determination of the nuclear deformation has some difficulty, e.g., one has to assume a simple structure model to extract the quadrupole deformation parameter from observed electric quadrupole transition strength [27]. Meanwhile, one promising measure that reflects the nuclear deformation is the nuclear matter radius. The nuclear deformation drastically changes the density profiles near the nuclear surface, leading to the enhancement of the nuclear radius. Measuring the total reaction or interaction cross section at high incident energy has been one of the standard methods and found various exotic phenomena such as halos [28, 29], developed neutron skin [30], in neutron-rich nuclei far from the β stability line. Recent developments of the radioactive beam facility extend the applicable mass region: Near dripline nucleus ^{29}F [31] and medium-mass nuclei beyond $N = 28$, $^{42-51}\text{Ca}$ [32]. One of the advantages of the total reaction cross section study is that the reaction theory has been well tested, allowing us to directly relate the cross section with the nuclear radius. Extracting nuclear size properties in the isotopic chain reveals structure changes due to excess neutrons. A systematic measurement of the cross sections for neutron-rich Ne and Mg clearly showed the evolution of the nuclear deformation with the help of reliable microscopic theoretical models [33–40]. The sudden increases of the total reaction cross section at the edge of the island of inversion near $N = 20$ were explained by the enhancement of the nuclear matter radius coming from a diffused nuclear surface induced by the strongly deformed nuclear state.

Extending this idea, in this paper, we study the nu-

* whoriuchi@nucl.sci.hokudai.ac.jp

clear shape of Ti, Cr, and Fe isotopes and discuss the possibility to determine the edge of the island of inversion near $N = 40$ using the total reaction cross sections. The territory of the island of inversion in this mass region has been explored in large-scale shell-model calculations [1]. The experimental indication that the border of the island of inversion goes beyond $N = 50$ was obtained in Ref. [41]. This work will show the utility of the total reaction cross section measurement to determine the location of the island of inversion in the nuclear landscape. In the Ti, Cr, and Fe isotopes, the nuclear deformation is strongly model dependent in $N = 34$ – 42 . Though most of the nuclei have a prolate shape, which is the so-called prolate dominance [42–44], some nuclei may exhibit oblate deformation. The shape of the wave function is determined with a delicate balance of the single-particle (s.p.) energies as the energy surface is soft with respect to the quadrupole deformation parameter γ in this mass region [45, 46]. Recently, the deformation effect on the nuclear density profile was discussed in detail [47]. The nuclear density was changed not only for the surface region but also the internal region by the nuclear deformation. Here we systematically investigate how those different density profiles are observed in the total reaction cross sections of Ti, Cr, and Fe isotopes at high incident energy.

The paper is organized as follows. In the next section, we briefly describe the microscopic structure and reaction models employed in this paper. Setups of the Skyrme-Hartree-Fock (HF) method and the Glauber model are given in Secs. II A and II B, respectively. We perform the HF calculations in the three-dimensional Cartesian coordinate, which can express any deformed shape. The model dependence is investigated by examining three sets of the Skyrme-type effective interactions. Using the density distributions obtained by the HF calculations, we compute the total reaction cross sections using the Glauber model without introducing any adjustable parameters. Section III presents our results. First, in Sec. III A we discuss structure changes of Ti, Cr, and Fe isotopes near $N = 40$, especially focusing on their nuclear deformation at around the neutron numbers $N = 34, 36$, and 40 by the microscopic mean-field model. A comparison of the calculated results with the experimental evaluation including recent data of the two-neutron separation energy is made. Following this comparison, we show in Sec. III B a systematic measurement of the total reaction cross sections becomes important to determine the location of the island of inversion near $N = 40$. Section III C discusses the role of the intruder s.p. orbits to determine the nuclear shape, especially focusing on the hexadecapole deformation. In Sec. III D, we address the possibility to determine these deformation parameters from the nuclear radius using a macroscopic model approach. The characteristics of the density profile of the nuclei in the island of inversion are elucidated. Conclusion is made in Sec. IV.

II. METHODS

A. Skyrme Hartree-Fock calculation in three-dimensional coordinate space

In this paper, we employ the Skyrme-HF calculation in three-dimensional (3D) coordinate representation. Since all details can be found in Refs. [38, 48, 49], we only give a minimum explanation for the present analysis. The ground-state wave function is expressed as the product of deformable s.p. orbits represented by the 3D Cartesian mesh which is flexible enough to describe higher-order multipole deformation, such as the hexadecapole one. We obtain these s.p. orbits fully self-consistently in the sphere of radius 20 fm based on the Skyrme energy density functional [50], in which the total energy is a functional of the intrinsic density $E[\rho_{\text{int}}]$ and is minimized using the imaginary-time method [51]. Three kinds of Skyrme parameter sets, SkM* [52], SLy4 [53] and SkI3 [54] are employed to obtain various density profiles. The SkM* interaction is one of the most used Skyrme interactions for nuclear structure calculation. The SLy4 interaction is constructed to reproduce a theoretical equation of state [55] and experimental data in a wide mass region, especially for neutron-rich nuclei. The SkI3 interaction is designed with attention to the reproducibility of s.p. levels of ^{208}Pb . There have been proposed a lot of the Skyrme interaction sets in the market [56]. Investigations of these three interactions are useful as they produce, e.g., different deformations and isovector density profiles [38, 47, 62]. The pairing interaction may change the nuclear deformation and induces the fractional occupation probability near the Fermi level. We remark that an elaborated beyond-mean-field calculation was done in this mass region [57]. The purpose of this study is to elucidate the effect of various nuclear deformations on the total reaction cross section. For the sake of simplicity, we only include the nuclear deformation, which is the most essential ingredient to determine the nuclear density profile. The pairing correlation is ignored in the present analysis as it induces further model dependence [58–62].

Once the ground-state wave function is obtained, the mean value of an operator $X(x, y, z)$ can be obtained by

$$\langle X \rangle = \frac{1}{A} \int_{-\infty}^{\infty} dx \int_{-\infty}^{\infty} dy \int_{-\infty}^{\infty} dz \rho_{\text{int}}(x, y, z) X(x, y, z). \quad (1)$$

The quadrupole deformation parameter is calculated as

$$\beta_2 = \sqrt{\beta_{20}^2 + \beta_{22}^2}, \quad (2)$$

where

$$\beta_{20} = \sqrt{\frac{\pi}{5} \frac{\langle 2z^2 - x^2 - y^2 \rangle}{\langle r^2 \rangle}}, \quad (3)$$

$$\beta_{22} = \sqrt{\frac{3\pi}{5} \frac{\langle x^2 - y^2 \rangle}{\langle r^2 \rangle}}, \quad (4)$$

with $r^2 = x^2 + y^2 + z^2$. We take z as the quantization axis and choose it as the largest (smallest) principal axis for prolate (oblate) deformation. We note that the ground-state wave function can be triaxially deformed as indicated by $\tan \gamma = \beta_{22}/\beta_{20}$ with $0^\circ < \gamma < 60^\circ$ in the present calculations.

The ground-state wave function may exhibit higher-order multipole deformation. We also calculate the hexadecapole deformation parameter defined by, e.g., see Ref. [63],

$$\beta_4 = \left[\sum_{m=-4}^4 \beta_{4m}^2 \right]^{\frac{1}{2}} \quad (5)$$

with

$$\beta_{4m} = \frac{4\pi}{3R^4} \langle r^4 Y_{4m} \rangle, \quad (6)$$

where $R = \sqrt{\frac{5}{3} \langle r^2 \rangle}$ is the nuclear radius. For later convenience, we define the hexadecapole moment operator as $Q_{4m} = r^4 Y_{4m}$, more explicitly with $m = 0$

$$Q_{40} = \frac{3}{16} \sqrt{\frac{1}{\pi}} (35z^4 - 30z^2r^2 + 3r^4). \quad (7)$$

B. Total reaction cross sections by Glauber theory

To bridge a gap between the density profiles obtained by the structure calculation and reaction observables, we need an appropriate reaction model. Here we consider the total reaction cross section on a carbon target at a high incident energy of more than a hundred MeV. The Glauber theory [64] formulated based on the adiabatic and eikonal approximations efficiently describes high energy nucleus-nucleus collisions of interest. In the Glauber formalism, the total reaction cross section is evaluated by

$$\sigma_R = \int d\mathbf{b} \left(1 - \left| e^{i\chi(\mathbf{b})} \right|^2 \right), \quad (8)$$

where the squared modulus of the phase-shift function $e^{i\chi(\mathbf{b})}$ is integrated over the impact parameter vector \mathbf{b} . The evaluation of $e^{i\chi(\mathbf{b})}$ is in general demanding because it involves multi-dimensional integration [65–67]. To incorporate the multiple scattering effect efficiently, here we employ the nucleon-target formalism (NTG) as given in Ref. [68]:

$$i\chi(\mathbf{b}) \approx - \int d\mathbf{r}^P \rho^P(\mathbf{r}^P) \times \left[1 - \exp \left\{ - \int d\mathbf{r}^T \rho^T(\mathbf{r}^T) \Gamma_{NN}(\mathbf{s}^P - \mathbf{s}^T + \mathbf{b}) \right\} \right] \quad (9)$$

where $\mathbf{r}^{P(T)} = (\mathbf{s}^{P(T)}, z^{P(T)})$ denotes the two dimensional coordinate of the projectile (target) nucleus perpendicular to the beam direction, $z^{P(T)}$. The NTG includes higher multiple-scattering terms and is known to

give a better description than optical-limit approximation [66, 69–71]; hence it has been employed as a standard tool to analyze the nuclear matter radius from measured cross sections [31, 33, 34, 72–74]. The theory requires the projectile $\rho^P(\mathbf{r}^P)$ and target density distributions $\rho^T(\mathbf{r}^T)$ and the profile function Γ_{NN} . We employ for the target nucleus ^{12}C the harmonic-oscillator type density [71] that reproduces the rms point-proton radius of ^{12}C , 2.33 fm [75]. The parameters of the profile function are taken from Ref. [76], which has been well tested, showing satisfactory descriptions of nucleus-nucleus collisions including short-lived nuclei, e.g., in Refs. [38, 40, 61, 66, 77]. We use the density distributions obtained from the HF calculations as the input projectile density distributions obtained by averaging over angles $\hat{\mathbf{r}} = (\theta, \phi)$ [38]

$$\rho^P(r) = \frac{1}{4\pi} \int d\hat{\mathbf{r}} \rho_{\text{int}}(r, \hat{\mathbf{r}}). \quad (10)$$

Note that in this work we treat all the physical quantities in the intrinsic frame, e.g., without angular momentum projection. The validity of this averaging treatment of the intrinsic density was confirmed in Ref. [37] through a comparison of the angular-momentum-projected density. Since the theory has no adjustable parameter, the total reaction cross section properly reflects the characteristics of the density profile obtained from the microscopic structure model.

III. RESULTS AND DISCUSSIONS

A. Nuclear quadrupole deformation and structure of Ti, Cr, and Fe isotopes

Figure 1 displays the calculated quadrupole deformation parameter of Ti, Cr, and Fe isotopes. For convenience, we use the familiar notation $-\beta_2$ for oblate shapes. As we see in the figure, the nuclear deformation is strongly interaction dependent in $N = 34$ –42 because the energy surface is soft with respect to the quadrupole deformation parameter γ in this mass region [45, 46] like as near $N = 20$. In fact, some nuclear states exhibit a triaxial shape: ^{62}Ti ($\gamma = 8.1^\circ$) for SkM*; ^{56}Cr ($\gamma = 14.3^\circ$), ^{60}Cr ($\gamma = 32.5^\circ$), and ^{64}Fe ($\gamma = 28.2^\circ$) for SLy4; and ^{54}Ti ($\gamma = 24.4^\circ$), ^{58}Ti ($\gamma = 43.5^\circ$), ^{60}Cr ($\gamma = 39.2^\circ$), ^{58}Fe ($\gamma = 17.2^\circ$), ^{62}Fe ($\gamma = 19.6^\circ$), and ^{64}Fe ($\gamma = 21.9^\circ$) for SkI3. Since the effect of the triaxiality is small for the enhancement of the nuclear radius as verified for Ne isotopes [37], quadrupole deformation with $0^\circ < \gamma < 30^\circ$ ($30^\circ < \gamma < 60^\circ$) is treated as prolate (oblate) in the figure for simplicity. The SkM* interaction tends to give strong deformation and the other interactions favor a less deformed shape. The most striking difference appears at $N \geq 34$ in which the prolate deformation grows for the SkM* interaction, while the others exhibit a less deformed shape. These differences can be attributed to the neutron s.p. level structure which can be explained in a similar way like in the island of inversion found near

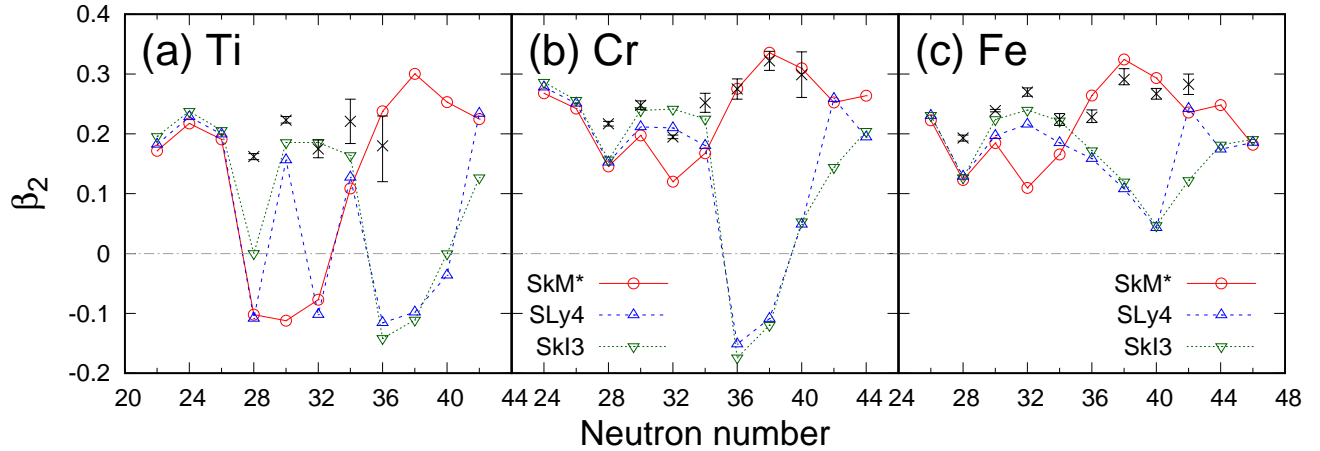


FIG. 1. Quadrupole deformation parameter β_2 of (a) Ti, (b) Cr, and (c) Fe isotopes as a function of the neutron number. Triaxial deformation with $0^\circ < \gamma < 30^\circ$ ($30^\circ < \gamma < 60^\circ$) is treated as prolate (oblate). The thin lines that connect theoretical results are to guide the eye. The cross symbols with an error bar indicate the empirical $|\beta_2|$ values evaluated by measured quadrupole transition strength [27].

$N = 20$. On moving $N = 34$ to 36 , the SkM* interaction makes the occupancy of the intruder orbit with the asymptotic quantum number $[nn_z\Lambda]\Omega = [440]1/2$ [78] stemming from the spherical $0g_{9/2}$ orbit and causes large prolate deformation. On the other hand, the SLy4 and SkI3 interactions increase the occupancy of the fp -shell orbit that results in much smaller β_2 values compared with the SkM* interaction. This is because the $0f_{5/2}$ - $0g_{9/2}$ level spacings for the SLy4 and SkI3 interactions are larger than that for the SkM* interaction. In fact, the calculated $0f_{5/2}$ - $0g_{9/2}$ level spacings in a spherical ^{90}Zr are 3.14 MeV, 4.99 MeV, and 7.09 MeV for the SkM*, SLy4, and SkI3 interactions, respectively. For the SLy4 and SkI3 interactions, since the $0f_{5/2}$ - $0g_{9/2}$ level spacings are large, the occupation of the $[440]1/2$ orbit, i.e., two-particle-two-hole (2p-2h) state, requires more energy than the energy that can be obtained from reduction, whereas the occupation of $[440]1/2$ orbit is realized with the SkM* interaction because of the small $0f_{5/2}$ - $0g_{9/2}$ level spacing. With the SkM* interaction, the largest deformation for Ti, Cr, and Fe isotopes at $N = 38$ is found with occupancy of the $[440]1/2$ and $[431]3/2$ orbits. At $N = 42$, the SLy4 interaction prefers additional occupancy of the orbit originated from the spherical $0g_{9/2}$ orbit, yielding different N -dependence of the nuclear deformation from the SkI3 interaction.

Since the nuclear structure is strongly depends on the Skyrme interaction employed, it is needed to verify these theoretical models through a comparison with experimental data. Figure 1 also displays the experimental evaluations of $|\beta_2|$ [27]. Though they are model dependent, relying on a simple collective model and only show the magnitude of the quadrupole deformation, their trend can be a guide to the nuclear deformation in this mass region. All the evaluated $|\beta_2|$ values exhibit large

quadrupole deformation $N \geq 36$. Their trends in Cr and Fe isotopes follow the results of the SkM* interaction. The SLy4 and SkI3 interactions are relatively less reproductive, predicting small collectivity for the Cr and Fe isotopes at $N = 36$ – 40 . In Ti isotopes, the magnitudes of the experimental evaluations are consistent with all the theoretical results because of their large uncertainties. Based on the systematical relation between the $|\beta_2|$ value and 2_1^+ energies, the low-lying 2_1^+ states in $^{60,62}\text{Ti}$ strongly show large quadrupole collectivity [22, 24]. Therefore, also in Ti isotopes, the SkM* interaction appears to be the most reasonable among the three interactions employed in this paper.

Since the nuclear deformation is sensitive to the energy levels near the Fermi level, we also compare our results with available experimental data of the two-neutron separation energy, which has intensively been studied in recent years. Figure 2 plots the two-neutron separation energies (S_{2n}) of Ti, Cr, and Fe isotopes. The experimental data is taken from the AME2020 database [79] and recent measurements [2, 80]. Overall agreement is obtained for all interactions employed here around $N = 34$ – 36 . In $N \gtrsim 34$, the SkI3 interaction tends to overestimate the data. The SLy4 interaction gives excellent agreement with the experimental data. The SkM* prediction nicely follows the experimental results in Ti isotopes but slightly overestimates the data in Cr and Fe isotopes. It appears that these effective interactions may not be accurate enough to describe the two-neutron separation energies in this mass region. We note, however, that the behavior does not follow that of the nuclear deformation though we see notable differences in the nuclear deformations as given in Figs. 1 and 5. On the other side, the S_{2n} trends may indicate that the enhancement of nuclear stability in this region could be affected not only from the

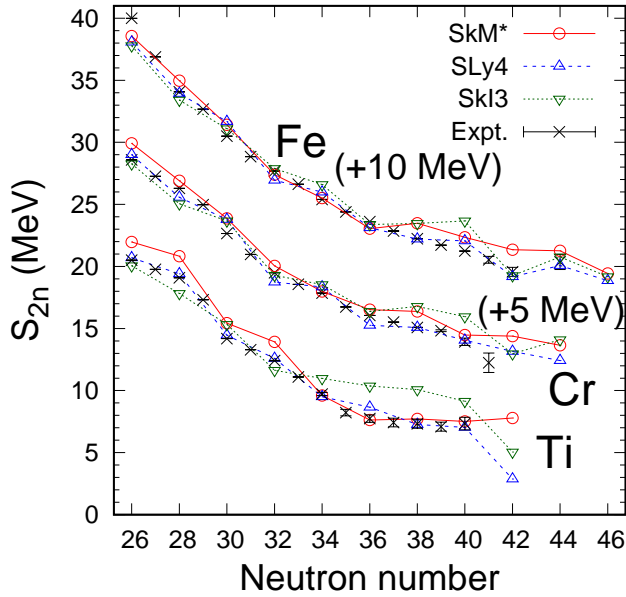


FIG. 2. Two-neutron separation energies of Ti, Cr, and Fe isotopes as a function of the neutron number. For clarity, 5 MeV for Cr and 10 MeV for Fe are respectively added to the results. The SkM*, SLy4, and SkI3 interactions are employed. The theoretical results for N even nuclei are plotted. The lines are to guide the eye. The experimental data are taken from Refs [2, 79, 80].

quadrupole deformation but also from the other effects, e.g., core swelling effect [47, 49].

B. Nuclear radii and total reaction cross sections in the island of inversion near $N = 40$

In Sec. III A, we overviewed the experimental situation on the structure of the Ti, Cr, and Fe isotopes and found that more experimental data is needed to establish the structure of those isotopes near $N = 40$. This motivates us to study the systematics of nuclear matter radii, which is sensitive to changes in the nuclear deformation. Figure 3 displays the root-mean-square (rms) matter radii of Ti, Cr, and Fe isotopes, $r_m = \sqrt{\langle r^2 \rangle}$. For the same Skyrme interaction, similar neutron-number dependence is predicted for the rms radii of those isotopes. However, the SkM* interaction exhibits different characteristics compared with the SLy4 and SkI3 ones. The SkM* predicts a sudden increase of the rms radius at $N = 34$, which is exactly a consequence of the onset of the intruder configuration and resultant nuclear deformation as given in Figs. 1 and 5. The nuclear radii obtained with the SLy4 and SkI3 interactions are largely enhanced not at $N = 34$ but at $N = 42$, which are comparable to those obtained with the SkM* interaction. These calculations clearly demonstrate a strong correlation between the oc-

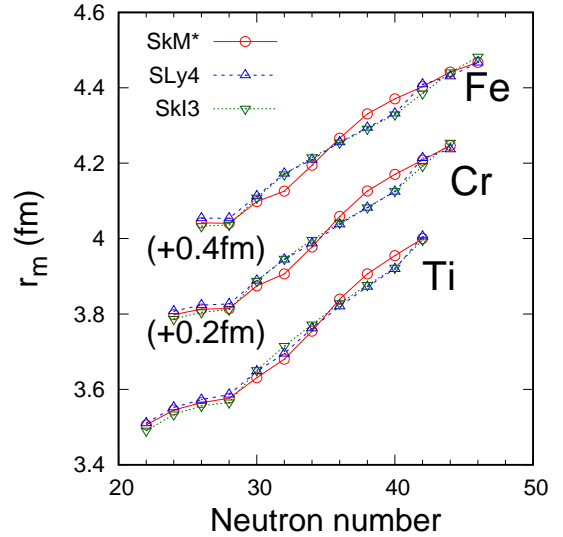


FIG. 3. Rms matter radii of Ti, Cr, and Fe isotopes as a function of the neutron number. For clarity, 0.2 and 0.4 fm are added to the results of Cr and Fe, respectively. The lines are to guide the eye. The SkM*, SLy4, and SkI3 interactions are employed.

cupation of the intruder configuration and the sudden increase of the nuclear radius. Therefore the edge of the island inversion can be observed experimentally as the sudden increase of the nuclear radius.

We examine how those differences are significant in cross section measurement. It is again stressed that the cross section calculations do not include adjustable parameters and the reliability of the adopted Glauber model has been established. As inputs to the theory are the density distributions obtained by the microscopic mean-field model, a systematic trend of the cross sections will properly describe the structure changes owing to the nuclear deformation. Figure 4 displays the total reaction cross sections on a carbon target. The incident energy is chosen as 240 MeV/nucleon, where the recent interaction cross section measurements were performed [31, 32]. The differences of the nuclear radii in $34 < N < 40$ are further emphasized in the total reaction cross sections using a carbon target because the carbon target has more sensitivity of the density profile beyond the nuclear surface [38, 81]. The cross section differences in $34 < N < 40$ are large at most more than 2%, which can be distinguished by measurement as its uncertainty is typically $\lesssim 1\%$ [31, 32]. A systematic cross section measurement of these isotopes is of cardinal importance because it will offer further evidence to determine the edge of the island of inversion near $N = 40$, where the strong deformation is predicted.

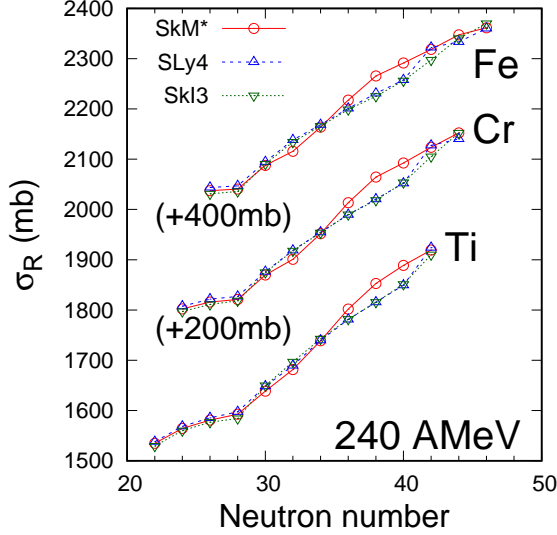


FIG. 4. Total reaction cross sections on a carbon target at 240 MeV/nucleon of Ti, Cr, and Fe isotopes as a function of the neutron number. For clarity, 200 and 400 mb are added to the results of Cr and Fe, respectively. The lines are to guide the eye. The SkM*, SLy4, and SkI3 interactions are employed.

C. Enhancement of hexadecapole deformation in the island of inversion

In this section, we discuss a unique feature of the nuclear deformation in the island of inversion. As discussed in Sec. III A, the occupation of the $[440]1/2$ orbital is a key to determine the quadrupole deformation in $N \gtrsim 34$. Because this is the most elongated along z axis, the occupancy may induce higher multipole deformation, i.e., hexadecapole deformation. Figure 5 plots the hexadecapole deformation parameter β_4 for Ti, Cr, and Fe isotopes. As we see in the figure, the β_4 value drastically increases at $N = 36$ for SkM* and $N = 42$ for SLy4 and SkI3, where the $[440]1/2$ orbit is occupied, i.e., the island inside.

To see the role of the elongated orbitals more quantitatively, we calculate the hexadecapole moment $\langle Q_{40} \rangle_{\text{sp}} = \langle [nn_z\Lambda] \Omega | Q_{40} | [nn_z\Lambda] \Omega \rangle$ for each s.p. orbit with the asymptotic quantum number $[nn_z\Lambda] \Omega$, and evaluate its cumulative sum in order of the s.p. energy from lowest to highest. We confirm that contributions of the other hexadecapole moments $\langle Q_{4m} \rangle_{\text{sp}}$ with $m \neq 0$ for all contributed s.p. orbits are negligible at most $\approx 1 \text{ fm}^4$, and thus $\langle Q_{40} \rangle_{\text{sp}}$ can be a good measure of the nuclear hexadecapole deformation. As we see in Sec. III A, the SkM* interaction can be the most favorable choice among the three interactions employed in this paper. Hereafter we only discuss the results obtained with the SkM* interaction otherwise noted. Figure 6 compares these obtained cumulative sum for $N = 38$ isotones, where the β_4 values

are largest. We sum up proton and neutron contributions simultaneously and hence only the neutron contribution is considered when the horizontal axis exceeds the proton number for each isotope. We find sudden increases at $N = 10, 22$, and 36 , which correspond to the occupation of the $[nn0]1/2$ orbital with $n = 2, 3$, and 4 , respectively. By further adding more neutrons to these neutron numbers, the hexadecapole moment decreases due to the occupation of less prolate orbitals. The $\langle Q_{40} \rangle_{\text{sp}}$ value tends to be large for prolately deformed orbitals and the smaller $\langle Q_{40} \rangle_{\text{sp}}$ value is found for oblate deformation, which can be expected from the definition of Q_{40} of Eq. (7). An approximate expression of the hexadecapole moment of the axially symmetric anisotropic harmonic-oscillator s.p. orbit with the asymptotic quantum number $[nn_z\Lambda]$ can be obtained as [82]

$$\begin{aligned} \langle nn_z\Lambda | Q_{40} | nn_z\Lambda \rangle &= \sqrt{\frac{9}{4\pi}} \left(\frac{\hbar^2}{2M\omega} \right)^2 \\ &\times \frac{3}{4} (27n_z^2 - 22n_zn + 3n^2 - \Lambda^2 - 6n_z - 2n), \end{aligned} \quad (11)$$

where M is the nucleon mass. By taking $\hbar\omega = 40A^{-1/3} \text{ MeV}$ with $A = 62$, we get $\langle nn0 | Q_{40} | nn0 \rangle = 43, 130$, and 260 fm^4 for $n = 2, 3$, and 4 , respectively, which roughly explain the trend obtained by the HF calculations: The corresponding increases of the cumulative $\langle Q_{40} \rangle_{\text{sp}}$ can be found in Fig. 6, whose values are $191.9/4=48.0$, $379.7/4=94.9$, and $332.7/2=166.3 \text{ fm}^4$ at the neutron/proton number 10, 24, and 36 for ^{62}Cr . The contribution of the $[440]1/2$ orbit is large and comparable to that of the $[330]1/2$ orbit despite that only 2 neutrons are occupied in this orbit, while in the $[220]1/2$ and $[330]1/2$ orbits additional 2 protons contribute to the hexadecapole moment.

For ^{64}Fe , an increase of the $\langle Q_{40} \rangle_{\text{sp}}$ value is rather milder than the others. Since the proton number $Z = 26$ fills the $[312]5/2$ orbit, in which $\langle 312 | Q_{40} | 312 \rangle$ value is negative, leading to smaller hexadecapole deformation in total. In the case of light nuclei, this proton configuration effect is more drastic. For example, for Ne, Mg, and Si in the island of inversion near $N = 20$, a sudden increase of the $\langle Q_{40} \rangle_{\text{sp}}$ value is also found when the $[330]1/2$ orbit is occupied at $N = 20$ for ^{30}Ne and ^{32}Mg . In fact, the β_4 value increases from $N = 18$ to 20 : from $\beta_4 = 0.03$ to 0.22 for Ne, from $\beta_4 = 0.00$ to 0.15 for Mg with the SkM* interaction. In contrast, for Si, the state exhibits a spherical shape because the proton number $Z = 14$ favors the oblate deformation. We also note that the large β_4 values for $N \approx Z$ of Ti, Cr, and Fe isotopes come from large hexadecapole moments due to the occupancy of the $[330]1/2$ orbit for both proton and neutron.

The density distribution of the deformed nuclear state offers a more intuitive picture of the role of the intruder orbits for the nuclear hexadecapole deformation. Figure 7 (a) draws a contour plot of the intrinsic density distribution of ^{58}Ti , where the last two neutrons fill in the $[440]1/2$ orbit with the SkM* interaction regarded as

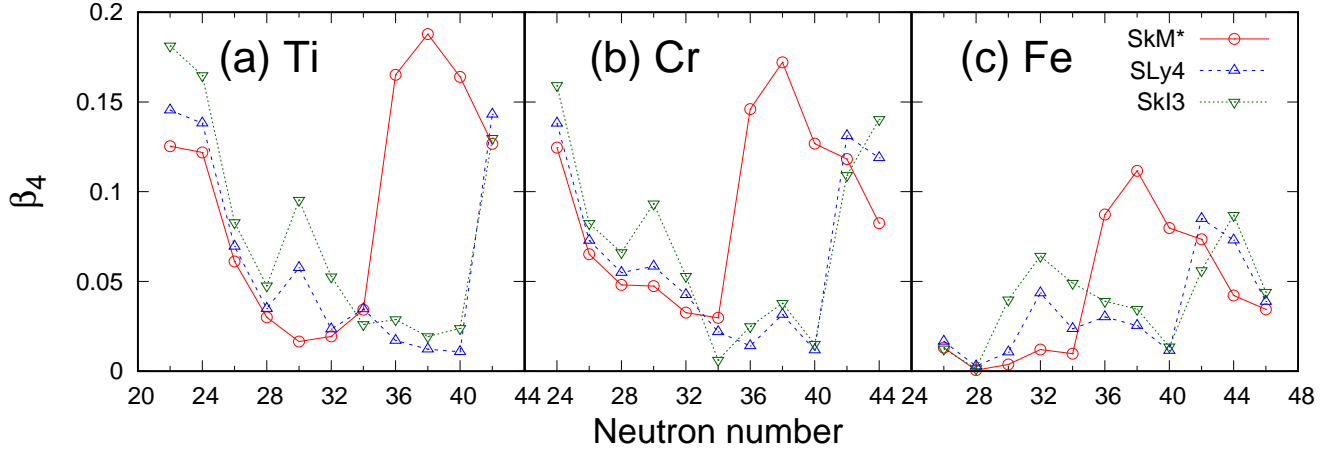


FIG. 5. Hexadecapole β_4 deformation parameters of (a) Ti, (b) Cr, and (c) Fe isotopes as a function of the neutron number.

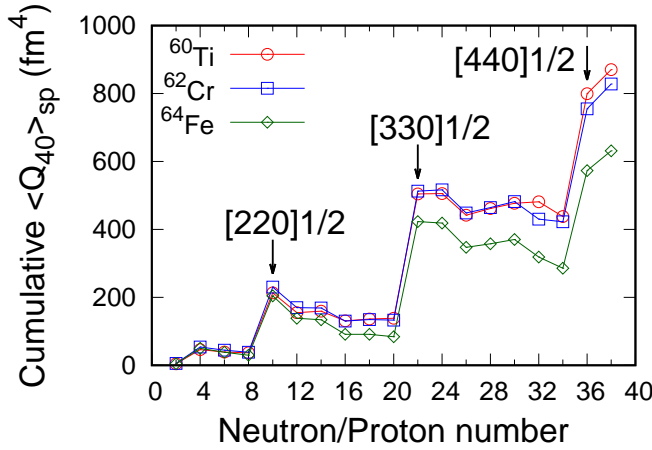


FIG. 6. Cumulative single-particle hexadecapole moment of the $N = 38$ isotones. The arrows indicate $N, Z = 10, 22$, and $N = 36$, where $[nn0]1/2$ orbit is occupied. The SkM* interaction is employed. See text for details.

the edge of the island of inversion. The nuclear radius R , $R(1 + \beta_2 Y_{20})$, and $R(1 + \beta_2 Y_{20} + \beta_4 Y_{40})$ are also plotted as a guide of the nuclear deformation. As clearly seen in the figure, a nuclear radius only with the quadrupole component ($1 + \beta_2 Y_{20}$) does not describe the total density distribution properly, while the nuclear radius that includes the hexadecapole component nicely follows the contour of the total density distribution, showing a “lemon” like shape. Figure 7 (b) displays the intrinsic densities of the sum of the $[220]1/2$, $[330]1/2$, and $[440]1/2$ orbits which give the three largest hexadecapole moments, and the remaining density subtracted from the total one is also plotted in Fig. 7 (c). The role of these elongated orbitals is apparent: The kurtosis of the total density distribution comes from these orbitals, while the remaining density

shows an almost spherical shape.

In general, the occupation of the $[nn0]1/2$ orbitals strongly enhances the hexadecapole deformation. A sudden increase of both the nuclear quadrupole and hexadecapole deformation is a strong indication of the edge of the island of inversion. Determination of the nuclear hexadecapole deformation will have of particular importance as it is sensitive to the occupation of the intruder $[nn0]1/2$ orbit. We note that the inclusion of the pairing correlations induces the fractional occupation number of the s.p. orbits near the Fermi level. An increase of the nuclear deformation parameters can be somewhat milder compared to the present results.

D. Quadrupole and hexadecapole deformation effects on nuclear radius and surface density profile

As we see in Sec. III C, the strong nuclear deformation is induced by the occupation of the intruder orbit and crucially affects the nuclear density profile near the nuclear surface. This appears simply as the enhancement of the nuclear radius. One may think that the deformation parameters can be extracted from the change of the nuclear radius. For small surface deformation with $1 + \sum_{\lambda \geq 2 \in \text{even}} \bar{\beta}_\lambda Y_{\lambda 0}$, the following formula has often been used to estimate the enhancement of the nuclear radius from the spherical limit [37, 83]

$$\Delta[r_{\text{mac}}^2] \approx \frac{5}{4\pi} \sum_{\lambda \geq 2 \in \text{even}} \bar{\beta}_\lambda^2. \quad (12)$$

We note that the hexadecapole deformation also induces the radius enhancement, which is usually ignored. However, we see the calculated β_4 values grow for $N > 34$ and become even comparable to the β_2 value. Since Eq. (12) could offer a direct relationship between the nuclear radius and deformation, it is worthwhile to investigate the

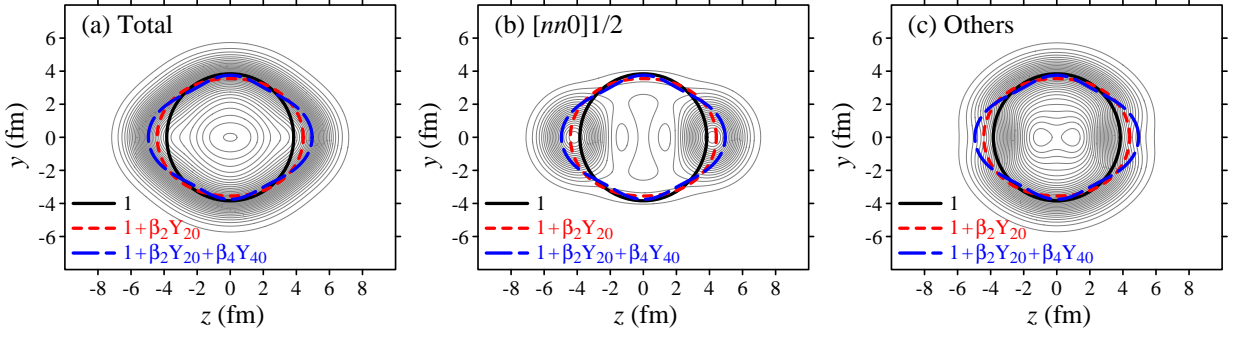


FIG. 7. Contour plot of the intrinsic density distribution of ^{58}Ti with the SkM* interaction, (a) total, (b) the sum of the $[220]1/2$, $[330]1/2$, and $[440]1/2$ orbits, and (c) the others. The sum of the density distributions of (b) and (c) corresponds to (a). The values at the peaks are (a) 0.184 (b) 0.096 fm^{-3} , and (c) 0.171 fm^{-3} . The contours are drawn in intervals of 0.005 fm^{-3} . Thick lines denote the nuclear radii considering spherical (1), quadrupole ($1 + \beta_2 Y_{20}$) deformation, and hexadecapole deformation ($1 + \beta_2 Y_{20} + \beta_4 Y_{40}$).

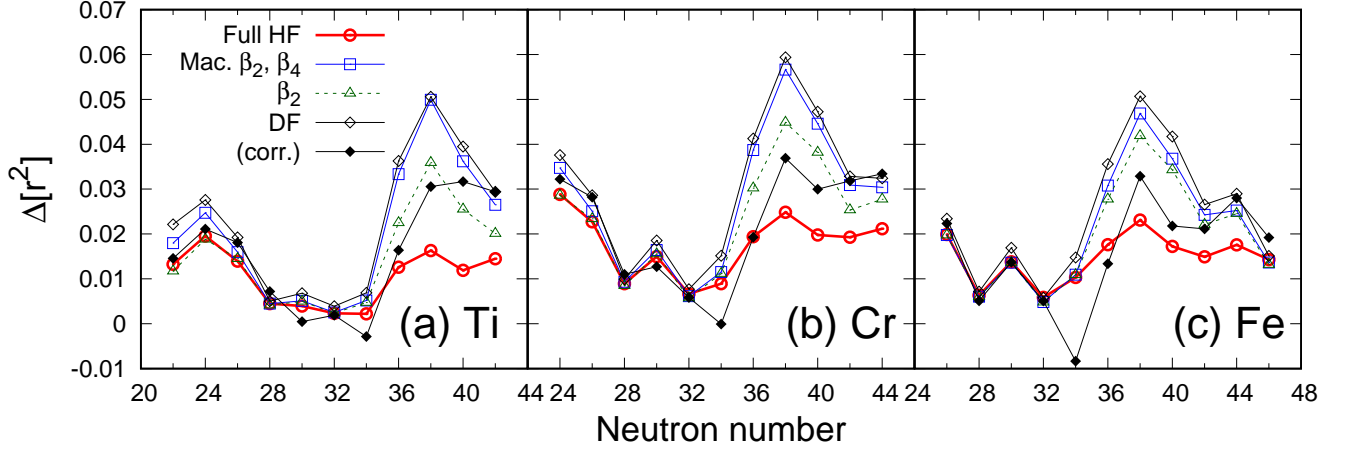


FIG. 8. Comparison of the relative difference of the square radii between the full and spherical constrained HF and the macroscopic formula of Eq. (12) including both the quadrupole and hexadecapole deformation parameters (β_2, β_4), and that only with β_2 for (a) Ti, (b) Cr, and (c) Fe isotopes. The SkM* interaction is employed for the HF calculations. The results with the deformed Fermi-type (DF) density distributions are also plotted. See text for details.

applicable range of the formula. To prepare the nuclear radii with a spherical limit, we calculate the nuclear radii obtained from the spherical constrained HF calculations using the filling approximation [47, 49]. Figure 8 compares the the relative difference between the mean-square matter radii of the full and spherical constrained HF calculations $\Delta[r_{\text{HF}}^2] = [r_{\text{m}}^2(\text{full}) - r_{\text{m}}^2(\text{sph.})]/r_{\text{m}}^2(\text{sph.})$ and $\Delta[r_{\text{mac.}}^2]$ with β_2, β_4 and only with β_2 . Here we regard β_λ as β_λ which is calculated from the HF intrinsic moments of Eqs. (2) and (5). The results with the SkM* interaction are shown as it exhibits the largest deformation among the other interactions. We find that the simple formula of Eq. (12) works well for $N \leq 34$ where $|\beta_2| \lesssim 0.2$. The β_4 contribution is minor as the β_4 value is also small in such small $|\beta_2|$ values. For $N \geq 36$, the square radii from the formula significantly overestimate the prediction of the

HF calculations. We also find large β_4 contributions accompanied with large quadrupole deformation $\beta_2 \gtrsim 0.2$, which induce a further deviation from the HF result. We also evaluate the hexacontatetrapole deformation parameters β_6 for all nuclei studied in this paper and confirm they are small, less than 0.01.

To incorporate the finite thickness of the nuclear surface which is ignored in Eq. (12), we consider a deformed Fermi-type (DF) density distribution

$$\rho_{\text{DF}}(r) = \frac{1}{4\pi} \int d\hat{r} \frac{\rho_0}{1 + \exp[(r - R(\theta))/a(\theta)]} \quad (13)$$

with axially symmetric deformed nuclear surface [82, 84]

$$R(\theta) = R'_0 [1 + \bar{\beta}_2 Y_{20}(\theta) + \bar{\beta}_4 Y_{40}(\theta)], \quad (14)$$

$$a(\theta) = a_0 \sqrt{1 + (\bar{\beta}_2 \nabla Y_{20}(\theta)|_{r=R(\theta)} + \bar{\beta}_4 \nabla Y_{40}(\theta)|_{r=R(\theta)})^2}. \quad (15)$$

First, $R'_0 = R_0$ and a_0 are determined by a least-square fitting of the spherical constrained HF density as prescribed in Refs. [85, 86] with a spherical limit $\bar{\beta}_2, \bar{\beta}_4 = 0$. The ρ_0 value is determined by the normalization $4\pi \int_0^\infty r^2 \rho_{\text{DF}}(r) dr = A$ for given R_0 and a_0 . Then $\bar{\beta}_2$ and $\bar{\beta}_4$ are determined to simultaneously reproduce the β_2 and β_4 values obtained from the HF calculation. The R'_0 value is uniquely determined by the volume conservation. Note that $\bar{\beta}_2$ and $\bar{\beta}_4$ correlate with the intrinsic deformation parameters β_2 and β_4 , that is, the surface deformation with $\bar{\beta}_2$ ($\bar{\beta}_4$) also induce β_4 (β_2) in the intrinsic density distribution defined in Eq. (13). Figure 8 shows these $\Delta[r^2]$ obtained with the DF density distributions. The results are almost identical with the ones obtained by the formula of Eq. (12) which assumes a sharp cut radius. This indicates that the surface density profile in the island of inversion cannot be explained by simple geometric deformation, i.e., the R_0 and a_0 values are no longer fixed parameters.

To quantify the changes of the surface density by the nuclear deformation, we evaluate the resultant nuclear surface diffuseness a in a spherical limit for each density distribution by using the same way described above. Note that the one with the spherical constrained HF corresponds to a_0 . Figure 9 plots the diffuseness parameters of the full HF, DF, and spherical constrained HF. The behavior of the a_0 value can be explained by considering a standard shell model filling [88]: The constant behavior is due to the occupation of the high- l orbits, $0f_{7/2}$, $0f_{5/2}$, and $0g_{9/2}$, while the low- l orbits, $1p_{3/2}$ and $1p_{1/2}$ in $28 \leq N \leq 34$ enhances the surface diffuseness. Compared with the diffuseness parameter extracted from the spherical constraint HF density, the a value of both HF and DF significantly enhanced by the nuclear deformation. The diffuseness parameters obtained by the DF distributions overestimate the full HF ones in $36 \leq N \leq 40$ despite that the DF results nicely agree with the HF results of the outside of the island of inversion. We calculate the $\Delta[r^2_{\text{m}}]$ value with the DF density by varying a_0 so as to reproduce the resultant diffuseness parameter a for the HF calculation. As shown in Fig. 8, the results are improved for $36 \leq N \leq 40$, implying the surface diffuseness changes beyond the geometrical one, while the systematic behavior due to the nuclear deformation is still present, and thus the nuclear deformation parameters can be constrained if one knows details about the nuclear density profile near the nuclear surface.

We note that this reduction of the diffuseness parameter is non-trivial because the nuclear deformation correction to the surface diffuseness is always positive. See Eq. (15). We remark that anti-correlation between the nuclear deformation and surface diffuseness was reported

in Ref. [84]. Reference [47] demonstrated that the nuclear deformation changes the density profile drastically and depends strongly on the shell structure near the Fermi level. From a microscopic point of view, in $N > 34$, the intruder $[440]1/2$ orbit induces the mixing of the spherical $0g_{9/2}$, $1d_{5/2}$, and $2s_{1/2}$ orbits. The lower angular momentum orbits, $1d_{5/2}$ and $2s_{1/2}$, play a role to enhance the nuclear radius owing to the large penetrability of the neutrons near the nuclear surface, while the $0g_{9/2}$ orbit suppresses the enhancement of the nuclear radius, which has the sharpest nuclear surface distribution. In fact, the neutron occupation number of the $0g_{9/2}$, $1d_{5/2}$ and $2s_{1/2}$ orbits was found to be 2.61, 0.95, and 0.04, respectively for ^{62}Cr [47]. We also remark that this large mixing of the $0g_{9/2}$ orbit is consistent with the finding of Ref. [1]. Consequently, resulting small surface diffuseness leads to the reduction of $\Delta[r^2_{\text{m}}]$ at $N \geq 36$. This shell effect induces the non-trivial change of the nuclear density profile, which cannot be explained from the simple geometric formulae. Similar behavior but a mixing of $1p_{3/2}$ and $0f_{7/2}$ at the island of inversion $N \gtrsim 20$ for Ne and Mg isotopes was reported in Ref. [86].

Figure 10 displays the total reaction cross sections calculated with the full HF, spherical HF, DF, diffuseness-corrected DF density distributions of Cr isotopes at 240 MeV/nucleon. For the sake of comparison, the cross section values with the DF density distributions are normalized to the full HF result at $N = 32$. The use of a carbon target has an advantage for studying details of the nuclear density profile, i.e., deformation effect on the nuclear surface because the density profile near the nuclear surface is more pronounced than a proton target [81]. In fact, we see a strong sensitivity in the cross section differences in $N \gtrsim 34$, which can be distinguished with the present experimental precision [31, 32]. Therefore, a systematic measurement of the total reaction cross sections in the isotope chains is strongly desired to get the structure information at the edge of and in the island of inversion. We also remark that proton-nucleus elastic scattering at forward angles is useful to obtain the nuclear surface diffuseness [85–87] as complementary evidence.

It should be noted that this finding opens the possibility of determining the hexadecapole deformation parameter from measurements of the total reaction cross sections. For example, one may assume the DF density distribution of Eq. (13), which includes four free parameters. They can be fixed by measurements of the total reaction cross sections at various incident energies and target nuclei. The parameters can further be constrained with information of the quadrupole deformation which can be deduced from a measurement of the electric-quadrupole transition strength. A careful investigation is necessary to extract these parameters quantitatively.

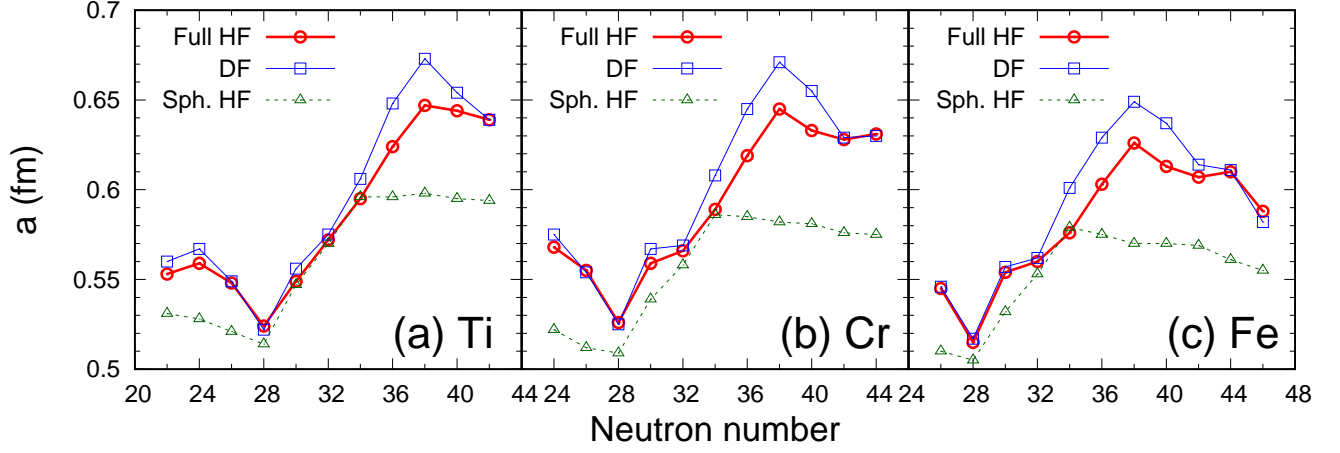


FIG. 9. Diffuseness parameter extracted from the full HF, deformed Fermi-type (DF), and spherical constrained HF densities for (a) Ti, (b) Cr, and (c) Fe isotopes. The SkM* interaction is employed. See text for details.

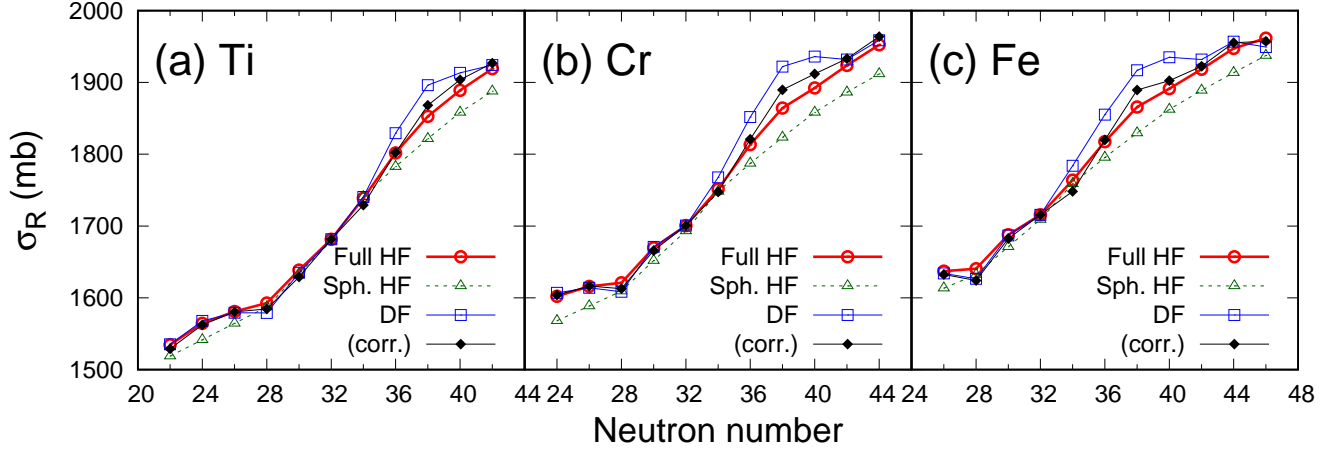


FIG. 10. Total reaction cross sections for (a) Ti, (b) Cr, and (c) Fe isotopes calculated with the full HF, spherical HF, deformed Fermi-type (DF), and diffuseness-corrected DF density distributions. Note that the cross sections with the DF density distributions are normalized to the full HF result at $N = 34$. The SkM* interaction is employed for the HF calculations.

IV. CONCLUSION

We have made a systematic analysis of nuclear deformation and discuss their effects on the nuclear radius or the total reaction cross section for even-even neutron-rich Ti, Cr, and Fe isotopes using reliable microscopic mean-field structure and reaction models. We have evaluated three standard sets of effective interactions for the mean-field calculations to examine the model dependence that comes from the nuclear deformation.

Using those obtained density distributions, we have calculated the total reaction cross sections without introducing any free parameter. In general, the cross section is enhanced if the nucleus exhibits strong deformation. We show that the enhancement is significant and can be iden-

tified with the recent experimental precision. Given the present comparison of the theoretical calculations with the available experimental evaluations of the quadrupole deformation and the recent data of the two-neutron separation energies, $N > 36$ is most likely in the island of inversion, where a sudden increase of nuclear deformation is predicted. The total reaction cross section offers more concrete evidence to determine the edge of the island of inversion near $N = 40$.

Characteristic nuclear deformation is found in the island of inversion: Strong hexadecapole deformation occurs simultaneously with the quadrupole deformation due to the occupation of the strongly deformed $[nn0]1/2$ Nilsson orbit. This characteristic structure drastically changes the density profile of these nuclei. However, we

find that the nuclear radius enhancement in the island of inversion cannot be explained by a simple geometrical deformation model, which implies non-trivial changes of the density profile that come from the shell structure near the Fermi level. This motivates us to study higher-order size properties of nuclei further than the nuclear radius, e.g., nuclear diffuseness [85], and higher radial moments [89].

The determination of both the nuclear radii and surface density profile will open a way to determine the deformation parameters of these nuclei, especially for the hexadecapole deformation. For this purpose, measurements of the total reaction cross sections for those iso-

topes at different incident energies and target nuclei are highly desired. Complementary information of experimental quadrupole deformation parameter and nuclear surface diffuseness can further help determine the higher-order term of the nuclear deformation.

ACKNOWLEDGMENTS

This work was in part supported by JSPS KAKENHI Grants No. 18K03635. We acknowledge the collaborative research program 2021, Information Initiative Center, Hokkaido University.

-
- [1] S. M. Lenzi, F. Nowacki, A. Poves, and K. Sieja, *Phys. Rev. C* **82**, 054301 (2010).
 - [2] S. Michimasa, M. Kobayashi, Y. Kiyokawa, S. Ota, R. Yokoyama, D. Nishimura, D. S. Ahn, H. Baba, G. P. A. Berg, M. Dozono *et al.*, *Phys. Rev. Lett.* **125**, 122501 (2020).
 - [3] E. K. Warburton, J. A. Becker, and B. A. Brown, *Phys. Rev. C* **41**, 1147 (1990).
 - [4] C. Thibault, R. Klapisch, C. Rigaud, A. M. Poskanzer, R. Prieels, L. Lessard, and W. Reisdorf, *Phys. Rev. C* **12**, 644 (1975).
 - [5] C. Détraz, D. Guillemaud, G. Huber, R. Klapisch, M. Langevin, F. Naulin, C. Thibault, L. C. Carraz, and F. Touchard, *Phys. Rev. C* **19**, 164 (1979).
 - [6] T. Motobayashi, Y. Ikeda, K. Ieki, M. Inoue, N. Iwasa, T. Kikuchi, M. Kurokawa, S. Moriya, S. Ogawa, H. Murakami *et al.*, *Phys. Lett. B* **346**, 9 (1995).
 - [7] A. Navin, D. W. Anthony, T. Aumann, T. Baumann, D. Bazin, Y. Blumenfeld, B. A. Brown, T. Glasmacher, P. G. Hansen, R. W. Ibbotson *et al.*, *Phys. Rev. Lett.* **85**, 266 (2000).
 - [8] H. Iwasaki, T. Motobayashi, H. Akiyoshi, Y. Ando, N. Fukuda, H. Fujiwara, Zs. Fülöp, K. I. Hahn, Y. Higurashi, M. Hirai *et al.*, *Phys. Lett. B* **481**, 7 (2000).
 - [9] H. Iwasaki, T. Motobayashi, H. Akiyoshi, Y. Ando, N. Fukuda, H. Fujiwara, Zs. Fülöp, K. I. Hahn, Y. Higurashi, M. Hirai *et al.*, *Phys. Lett. B* **491**, 8 (2000).
 - [10] T. Glasmacher, B. A. Brown, M. J. Chromik, P. D. Cottle, M. Fauerbach, R. W. Ibbotson, K. W. Kemper, D. J. Morrissey, H. Scheit, D. W. Sklenicka, and M. Steiner, *Phys. Lett. B* **395**, 163 (1997).
 - [11] F. Sarazin, H. Savajols, W. Mittig, F. Nowacki, N. A. Orr, Z. Ren, P. Roussel-Chomaz, G. Auger, D. Baiborodin, A. V. Belozorov *et al.*, *Phys. Rev. Lett.* **84**, 5062 (2000).
 - [12] B. Bastin, S. Grévy, D. Sohler, O. Sorlin, Zs. Dombrádi, N. L. Achouri, J. C. Angélique, F. Azaiez, D. Baiborodin, R. Borcea *et al.*, *Phys. Rev. Lett.* **99**, 022503 (2007).
 - [13] S. Takeuchi, M. Matsushita, N. Aoi, P. Doornenbal, K. Li, T. Motobayashi, H. Scheit, D. Steppenbeck, H. Wang, H. Baba *et al.*, *Phys. Rev. Lett.* **109**, 182501 (2012).
 - [14] B. A. Brown, *Prog. Part. Nucl. Phys.* **47**, 517 (2001).
 - [15] S. Naimi, G. Audi, D. Beck, K. Blaum, Ch. Böhm, Ch. Borgmann, M. Breitenfeldt, S. George, F. Herfurth, A. Herlert *et al.*, *Phys. Rev. C* **86**, 014325 (2012).
 - [16] Z. Meisel, S. George, S. Ahn, D. Bazin, B. A. Brown, J. Browne, J. F. Carpino, H. Chung, R. H. Cyburt, A. Estradé *et al.*, *Phys. Rev. C* **93**, 035805 (2016).
 - [17] M. Mougeot, D. Atanasov, K. Blaum, K. Chrysalidis, T. D. Goodacre, D. Fedorov, V. Fedosseev, S. George, F. Herfurth, J. D. Holt *et al.*, *Phys. Rev. Lett.* **120**, 232501 (2018).
 - [18] M. Hannawald, T. Kautzsch, A. Wöhr, W. B. Walters, K.-L. Kratz, V. N. Fedoseyev, V. I. Mishin, W. Böhmer, B. Pfeiffer, V. Sebastian *et al.*, *Phys. Rev. Lett.* **82**, 1391 (1999).
 - [19] O. Sorlin, C. Donzaud, F. Nowacki, J. C. Angélique, F. Azaiez, C. Bourgeois, V. Chiste, Z. Dlouhy, S. Grévy, D. Guillemaud-Mueller *et al.*, *Eur. Phys. J. A* **16**, 55 (2003).
 - [20] P. Adrich, A. M. Amthor, D. Bazin, M. D. Bowen, B. A. Brown, C. M. Campbell, J. M. Cook, A. Gade, D. Galaviz, T. Glasmacher *et al.*, *Phys. Rev. C* **77**, 054306 (2008).
 - [21] N. Aoi, E. Takeshita, H. Suzuki, S. Takeuchi, S. Ota, H. Baba, S. Bishop, T. Fukui, Y. Hashimoto, H. J. Ong *et al.*, *Phys. Rev. Lett.* **102**, 012502 (2009).
 - [22] A. Gade, R. V. F. Janssens, D. Weisshaar, B. A. Brown, E. Lunderberg, M. Albers, V. M. Bader, T. Baugher, D. Bazin, J. S. Berryman *et al.*, *Phys. Rev. Lett.* **112**, 112503 (2014).
 - [23] K. Wimmer, F. Recchia, S. M. Lenzi, S. Riccetto, T. Davinson, A. Estrade, C. J. Griffin, S. Nishimura, F. Nowacki, V. Phong *et al.*, *Phys. Lett. B* **792**, 16 (2019).
 - [24] M. L. Cortés, W. Rodriguez, P. Doornenbal, A. Obertelli, J. D. Holt, S. M. Lenzi, J. Menéndez, F. Nowacki, K. Ogata, A. Poves *et al.*, *Phys. Lett. B* **800**, 135071 (2020).
 - [25] J. Ljungvall, A. Görgen, A. Obertelli, W. Korten, E. Clément, G. de France, A. Bürger, J.-P. Delaroche, A. Dewald, A. Gadea *et al.*, *Phys. Rev. C* **81**, 061301(R) (2010).
 - [26] H. L. Crawford, R. M. Clark, P. Fallon, A. O. Macchiavelli, T. Baugher, D. Bazin, C. W. Beausang, J. S. Berryman, D. L. Bleuel, C. M. Campbell *et al.*, *Phys. Rev. Lett.* **110**, 242701 (2013).
 - [27] B. Pritychenko, M. Birch, B. Singh, and M. Horoi, *At. Data Nucl. Data Tables* **107**, 1 (2016).
 - [28] I. Tanihata, H. Hamagaki, O. Hashimoto, Y. Shida, N. Yoshikawa, K. Sugimoto, O. Yamakawa, T. Kobayashi, and N. Takahashi, *Phys. Rev. Lett.* **55**, 2676 (1985).

- [29] I. Tanihata, H. Savajols, and R. Kanungo, Prog. Part. Nucl. Phys. **68**, 215 (2013), and references therein.
- [30] T. Suzuki, H. Geissel, O. Bochkarev, L. Chulkov, M. Golovkov, D. Hirata, H. Irnich, Z. Janas, H. Keller, T. Kobayashi *et al.*, Phys. Rev. Lett. **75**, 3241 (1995).
- [31] S. Bagchi, R. Kanungo, Y. K. Tanaka, H. Geissel, P. Doornenbal, W. Horiuchi, G. Hagen, T. Suzuki, N. Tsunoda, D. S. Ahn *et al.*, Phys. Rev. Lett. **124**, 222504 (2020).
- [32] M. Tanaka, M. Takechi, M. Fukuda, D. Nishimura, T. Suzuki, Y. Tanaka, T. Moriguchi, D. S. Ahn, A. Aimagambetov, M. Amano *et al.*, Phys. Rev. Lett. **124**, 102501 (2020).
- [33] M. Takechi, T. Ohtsubo, M. Fukuda, D. Nishimura, T. Kuboki, T. Kubo, T. Suzuki, T. Yamaguchi, A. Ozawa, T. Moriguchi, H. Ooishi, Phys. Lett. **B 707**, 357 (2012).
- [34] M. Takechi, S. Suzuki, D. Nishimura, M. Fukuda, T. Ohtsubo, M. Nagashima, T. Suzuki, T. Yamaguchi, A. Ozawa, T. Moriguchi *et al.*, Phys. Rev. C **90**, 061305(R) (2014).
- [35] K. Minomo, T. Sumi, M. Kimura, K. Ogata, Y. R. Shimizu, and M. Yahiro, Phys. Rev. C **84**, 034602 (2011).
- [36] K. Minomo, T. Sumi, M. Kimura, K. Ogata, Y. R. Shimizu, and M. Yahiro, Phys. Rev. Lett. **108**, 052503 (2012).
- [37] T. Sumi, K. Minomo, S. Tagami, M. Kimura, T. Matsumoto, K. Ogata, Y. R. Shimizu, and M. Yahiro, Phys. Rev. C **85**, 064613 (2012).
- [38] W. Horiuchi, T. Inakura, T. Nakatsukasa, and Y. Suzuki, Phys. Rev. C **86**, 024614 (2012).
- [39] S. Watanabe, K. Minomo, M. Shimada, S. Tagami, M. Kimura, M. Takechi, M. Fukuda, D. Nishimura, T. Suzuki, T. Matsumoto *et al.*, Phys. Rev. C **89**, 044610 (2014).
- [40] W. Horiuchi, T. Inakura, T. Nakatsukasa, and Y. Suzuki, JPS Conf. Proc. **6**, 030079 (2015).
- [41] C. Santamaria, C. Louchart, A. Obertelli, V. Werner, P. Doornenbal, F. Nowacki, G. Authalet, H. Baba, D. Calvet, F. Château, Phys. Rev. Lett. **115**, 192501 (2015).
- [42] K. Kumar, Phys. Rev. C **1**, 369 (1970).
- [43] N. Tajima and N. Suzuki, Phys. Rev. C **64**, 037301 (2001).
- [44] I. Hamamoto and B. R. Mottelson, Phys. Rev. C **79**, 034317 (2009).
- [45] K. Yoshida and N. Hinohara, Phys. Rev. C **83**, 061302(R) (2011).
- [46] K. Sato, N. Hinohara, K. Yoshida, T. Nakatsukasa, M. Matsuo, and K. Matsuyanagi, Phys. Rev. C **86**, 024316 (2012).
- [47] W. Horiuchi and T. Inakura, Prog. Theor. Exp. Phys. **2021**, 103D02 (2021).
- [48] T. Inakura, H. Imagawa, Y. Hashimoto, S. Mizutori, M. Yamagami K. Matsuyanagi, Nucl. Phys. **A 768**, 61 (2006).
- [49] W. Horiuchi and T. Inakura, Phys. Rev. C **101**, 061301(R) (2020).
- [50] D. Vautherin and D. M. Brink, Phys. Rev. C **5**, 626 (1972).
- [51] K. T. R. Davies, H. Flocard, S. Krieger, and M.S. Weiss, Nucl. Phys. **A 342**, 111 (1980).
- [52] J. Bartel, P. Quentin, M. Brack, C. Guet, and H. Håkansson, Nucl. Phys. **A 386**, 79 (1982).
- [53] E. Chanbanat, P. Bonche, P. Haensel, J. Mayer, and R. Schaeffer, Nucl. Phys. **A 627**, 710 (1997).
- [54] P.-G. Reinhard and H. Flocard, Nucl. Phys. **A 584**, 467 (1995).
- [55] A. Akmal, V. R. Pandharipande, and D.G. Ravenhall, Phys. Rev. C **58**, 1804 (1998).
- [56] M. Dutra, O. Lourenço, J. S. Sá Martins, A. Delfino, J. R. Stone, and P. D. Stevenson, Phys. Rev. C **85**, 035201 (2012).
- [57] T. R. Rodríguez, A. Poves, and F. Nowacki, Phys. Rev. C **93**, 054316 (2016).
- [58] J. -P. Delaroche, M. Girod, J. Libert, H. Goutte, S. Hilaire, S. Péru, N. Pillet, and G. F. Bertsch, Phys. Rev. C **81**, 014303 (2010).
- [59] M. V. Stoitsov, J. Dobaczewski, W. Nazarewicz, S. Pittel, and D. J. Dean, Phys. Rev. C **68**, 054312 (2003).
- [60] S. A. Changizi and C. Qi, Phys. Rev. C **91**, 024305 (2015).
- [61] W. Horiuchi, S. Hatakeyama, S. Ebata, and Y. Suzuki, Phys. Rev. C **93**, 044611 (2016).
- [62] W. Horiuchi, S. Ebata, and K. Iida, Phys. Rev. C **96**, 035804 (2017).
- [63] M. Bender, P.-H. Heenen, P.-G. Reinhard, Rev. Mod. Phys. **75**, 121 (2003).
- [64] R. J. Glauber, *Lectures in Theoretical Physics*, edited by W. E. Brittin and L. G. Dunham (Interscience, New York, 1959), Vol. 1, p.315.
- [65] K. Varga, S. C. Pieper, Y. Suzuki, and R. B. Wiringa, Phys. Rev. C **66**, 034611 (2002).
- [66] T. Nagahisa and W. Horiuchi, Phys. Rev. C **97**, 054614 (2018).
- [67] S. Hatakeyama and W. Horiuchi, Nucl. Phys. **A 985**, 20 (2019).
- [68] B. Abu-Ibrahim and Y. Suzuki, Phys. Rev. C **61**, 051601(R) (2000).
- [69] W. Horiuchi and Y. Suzuki, Phys. Rev. C **74**, 034311 (2006).
- [70] W. Horiuchi, Y. Suzuki, B. Abu-Ibrahim, and A. Kohama, Phys. Rev. C **75**, 044607 (2007); *ibid* **76**, 039903(E) (2007).
- [71] B. Abu-Ibrahim, S. Iwasaki, W. Horiuchi, A. Kohama, and Y. Suzuki, J. Phys. Soc. Jpn., Vol. 78, 044201 (2009).
- [72] M. Takechi, M. Fukuda, M. Mihara, K. Tanaka, T. Chinda, T. Matsumasa, M. Nishimoto, R. Matsumiya, Y. Nakashima *et al.*, Phys. Rev. C **79**, 061601(R) (2009).
- [73] R. Kanungo, A. Prochazka, W. Horiuchi, C. Nociforo, T. Aumann, D. Boutin, D. Cortina-Gil, B. Davids, M. Diakaki, F. Farinon *et al.*, Phys. Rev. C **83**, 021302(R) (2011).
- [74] R. Kanungo, A. Prochazka, W. Horiuchi, C. Nociforo, T. Aumann, D. Boutin, D. Cortina-Gil, B. Davids, M. Diakaki, F. Farinon *et al.*, Phys. Rev. C **83**, 021302(R) (2011).
- [75] I. Angeli and K. P. Marinova, At. Data Nucl. Data Tables **99**, 69 (2013).
- [76] B. Abu-Ibrahim, W. Horiuchi, A. Kohama, and Y. Suzuki, Phys. Rev. C **77**, 034607 (2008); *ibid* **80**, 029903(E) (2009); **81**, 019901(E) (2010).
- [77] W. Horiuchi, Y. Suzuki, P. Capel, and D. Baye, Phys. Rev. C **81**, 024606 (2010).
- [78] S. G. Nilsson, Mat. Fys. Medd. Dan. Vid. Selsk. **29**, pp.1-69 (1955).
- [79] M. Wang, W. J. Huang, F. G. Kondev, G. Audi, S. Naimi, Chin. Phys. C **45**, 030003 (2021).
- [80] Z. Meisel, S. George, S. Ahn, D. Bazin, B. A. Brown, J. Browne, J. F. Carpino, H. Chung, R. H. Cyburt, A. Estradé *et al.*, Phys. Rev. C **101**, 052801(R) (2020).

- [81] W. Horiuchi, Y. Suzuki, and T. Inakura, Phys. Rev. C **89**, 011601(R) (2014).
- [82] A. Bohr and B. R. Mottelson, Nuclear Structure, Vol. II (W. A. Benjamin, New York, 1975).
- [83] A. Bohr and B. R. Mottelson, Nuclear Structure, Vol. I (W. A. Benjamin, New York, 1975).
- [84] G. Scamps, D. Lacroix, G. G. Adamian, and N. V. Antonenko, Phys. Rev. C **88**, 064327 (2013).
- [85] S. Hatakeyama, W. Horiuchi, and A. Kohama, Phys. Rev. C **97**, 054607 (2018).
- [86] V. Choudhary, W. Horiuchi, M. Kimura, and R. Chatterjee, Phys. Rev. C **104**, 054313 (2021).
- [87] V. Choudhary, W. Horiuchi, M. Kimura, and R. Chatterjee, Phys. Rev. C **102**, 034619 (2020).
- [88] W. Horiuchi, Prog. Theor. Exp. Phys. (2021), doi: 10.1093/ptep/ptab136.
- [89] H. Kurasawa and T. Suzuki, Prog. Theor. Exp. Phys. **2019**, 113D01 (2019).